Worm-Like Superparamagnetic Nanoparticle Clusters for Enhanced Adhesion and Magnetic Resonance Relaxivity

Cartney E. Smith[†], JuYeon Lee[‡], Yongbeom Seo[†], Nicholas Clay[†], Jooyeon Park[†], Artem Shkumatov[§], Dawn Ernenwein[‡], Mei-Hsiu Lai[†], Sanjay Misra[∥], Charles E. Sing[†], Brenda Andrade[‡], Steven C. Zimmerman[*,‡], Hyunjoon Kong[*,†,⊥]

[†]Department of Chemical and Biomolecular Engineering, University of Illinois at Urbana–Champaign, Urbana, Illinois 61801, United States

[‡]Department of Chemistry, University of Illinois at Urbana–Champaign, Urbana, Illinois 61801, United States

[§]Department of Pathobiology, College of Veterinary Medicine, University of Illinois at Urbana–Champaign, Urbana, Illinois 61801, United States

[∥]Department of Radiology, Mayo Clinic, Rochester, Minnesota 55905, United States

[⊥]Department of Bioengineering, Institute for Genomic Biology, University of Illinois at Urbana–Champaign, Urbana, Illinois 61801, United States

Abstract

Nanosized bioprobes that can highlight diseased tissue can be powerful diagnostic tools. However, a major unmet need is a tool with adequate adhesive properties and contrast-to-dose ratio. To this end, this study demonstrates that targeted superparamagnetic nanoprobes engineered to present a worm-like shape and hydrophilic packaging enhance both adhesion efficiency to target substrates and magnetic resonance (MR) sensitivity. These nanoprobes were prepared by the controlled self-assembly of superparamagnetic iron oxide nanoparticles (SPIONs) into worm-like superstructures using glycogen-like amphiphilic hyperbranched polyglycerols functionalized with peptides capable of binding to defective vasculature. The resulting worm-like SPION clusters presented binding affinity to the target substrate 10-fold higher than that of spherical ones and T_2 molar MR relaxivity 3.5-fold higher than that of conventional, single SPIONs. The design principles discovered for these nanoprobes should be applicable to a range of other diseases where improved diagnostics are needed.
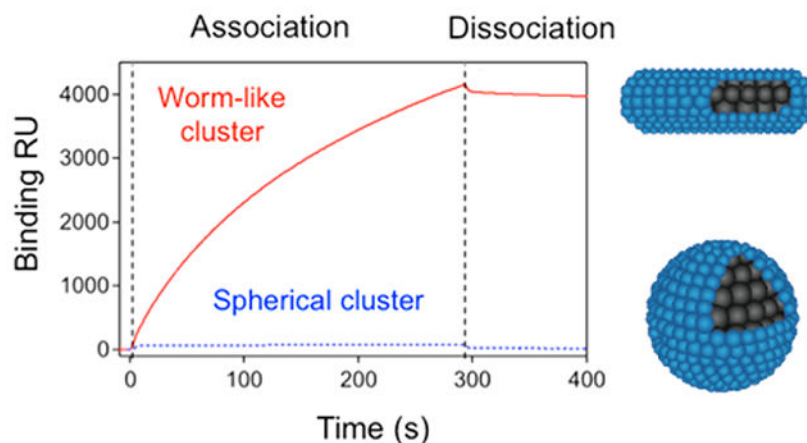
Graphical Abstract

1. INTRODUCTION

Early diagnosis is a critical element in the complete and successful treatment of multiple acute, chronic, and malignant diseases. As such, a highly active but challenging area of research is focused on the development of smart beacons that can anchor exclusively to diseased tissue following systemic administration and provide high contrast bioimages.[1–5] Toward this end, nonspherical nanoparticles have emerged as preferred carriers of bioimaging contrast agents because of their ability to adhere to target tissues with affinity greater than that of their spherical counterparts.[6,7]

A common method of controlling nanoparticle shape is to modulate the intermolecular packing parameter of self-assembling amphiphilic molecules.[8–10] However, attaining an optimal packing parameter to achieve a desired, elongated morphology often requires a large hydrophobic component.[11–15] As a consequence, the resulting nanoprobes have significantly limited functionality and contrast efficiency because the large hydrophobic layer surrounding the cargo substantially reduces the interaction between the nanoprobe and surrounding biological fluid. This is of particular importance when designing nanoprobes to carry contrast agents for magnetic resonance imaging (MRI), which rely mechanistically on the access of contrast agents to water molecules in the target tissue.[16]

We hypothesized that an MR-based nanoprobe with a highly elongated morphology, a hydrophilic surface coating, and peptides capable of binding diseased tissue would present superior tissue binding affinity without reducing relaxivity. We examined this hypothesis by changing the shape of clustered superparamagnetic iron oxide nanoparticles (SPIONs), a T_2 MR contrast agent, from spherical to nonspherical using amphiphilic hyperbranched polyglycerols (HPGs) with a binary molecular weight distribution. Specifically, HPG with molecular weights of 3000 and 50 000 g/mol were mixed at different ratios to modulate

the packing density of the SPIONs, in turn changing the curvature of the cluster. The HPG was specifically chosen to surround the SPION clusters because its unique glycogen-like hyperbranched architecture presents a larger number of hydroxyl groups in a small volume, thus maximizing the hydrophilicity of the polymers. The HPG further provided a platform to which oligopeptides containing the VHPKQHR sequence, termed VHPKQHR peptide, could be chemically coupled. This peptide bears homology to the very late antigen-4 (VLA-4) found on leukocytes and therefore binds with vascular cell adhesion molecule-1 (VCAM-1), which is overexpressed by inflamed endothelial cells.[17]

We assessed the ability of the bioactive, worm-like SPION nanoclusters to adhere to and serve as nanobeacons of vascular defects by examining the nanocluster morphology with transmission electron microscopy (TEM), measuring the MR relaxivity of phantom models of SPION clusters, and quantifying nanocluster binding kinetics in vitro using surface plasmon resonance (SPR) spectroscopy. Spherical SPION nanoclusters prepared with HPG with a single molecular weight were used as a control.

2. MATERIALS AND METHODS

2.1. Synthesis of Alkylated HPG.

All materials were purchased from Sigma-Aldrich unless otherwise noted. HPG was synthesized and alkylated according to the procedure previously described.[18] Characterization of HPG and alkylated HPG is shown in Figures S1 and S2, respectively.

2.2. Conjugation of VCAM-1 Binding Peptides to HPG.

Alkylated HPG, HPG_{3k}-g-$C_{18}(3)$ (107.3 mg, 1 equiv), was dried under high vacuum overnight 1 day before the reaction. Dried HPG was then dissolved in anhydrous DMF (20 mL), to which distilled triethylamine (467.5 μL, 312 equiv) was added. The reaction flask was placed in an ice bath before the addition of methacryloyl chloride to cool the reaction solution. Methacryloyl chloride (359 μL, 156 equiv) was then added dropwise, and the reaction continued to stir at room temperature for 24 h. The reaction of methacryloyl chloride with hydroxyl groups in HPG was monitored by ^{1}H NMR of an aliquot of the reaction mixture. Then, the peptide solution in DMF (137.8 mg, 6 equiv, H_2N-VHPKQHRGGSWGC-$CONH_2$, Mimotopes, Victoria, Australia) was added to the reaction flask, and the reaction continued for another 24 h at 60 °C. The thiol group in cysteine reacted with the methacryloyl group on HPG via Michael addition. Afterward, the remaining methacryloyl groups on HPG were quenched with 3-mercaptopropane-1,2-diol. The reaction solution was then dialyzed for 2 days against an aqueous NaCl solution (10 g/L followed by 5 g/L) and then for 1 day against deionized water. The amount of peptide conjugated to HPG_{3k}-g-$C_{18}(3)$ was determined by UV absorbance at 280 nm to be 0.457 mmol/g polymer.

2.3. Formation of SPION Nanoclusters.

Hydrophobic SPIONs stabilized with oleic acid were suspended in chloroform at 10 mg/mL.[19] To form nanoclusters, SPIONs were sonicated with varying ratios of alkylated HPG_{50k} to HPG_{3k} dissolved in water. Removal of the chloroform was then accomplished by rotary evaporation, and the resultant clusters were purified from unclustered materials

by centrifugation. For the assembly of biofunctionalized SPION clusters, peptide-conjugated HPG_{3k}-g-C_{18} was incorporated with either HPG_{50k}-g-C_{18} or unmodified HPG_{3k}-g-C_{18} at a 3:1 molar ratio to prepare worm-like and spherical clusters, respectively.

2.4. Microscopic Analysis of Nanoclusters.

HPG-SPION nanoclusters were imaged with a JEOL 2100 transmission electron microscope (JEOL 2100 cryo TEM). The accelerating voltage was set at 200 kV, and specimens were air-dried on a holey carbon-coated copper grid. Quantitative analysis was conducted with ImageJ software. Approximately 50 clusters were analyzed per condition. Additionally, to support the stability of worm-like clusters in serum, clusters were incubated at 37 °C in a solution of phosphate buffered saline (PBS) containing 10% bovine serum for 30 min, followed by analysis by TEM.

2.5. Determination of Kinetic Binding Parameters for Adhesion of SPION Nanoclusters onto a Target Substrate.

The targeted binding of peptide-conjugated nanoclusters was measured with a Biacore 3000 (GE Healthcare, United States). A gold sensor chip was modified with 11-mercaptoundecanoic acid to present reactive carboxylic acid groups on the chip surface. The carboxyl groups were then activated by flowing 1-ethyl-3-(3-(dimethylamino)propyl)carbodiimide (EDC) and N-hydroxysuccinimide (NHS) over the chip, followed by a recombinant human VCAM-1 (R&D systems) to attach the protein to the gold surface. SPION nanoclusters functionalized with VCAM-1 binding peptides and unmodified SPION nanoclusters at an iron concentration of 420 μM in PBS were then flowed over the surface at a rate of 5 μL/min to measure association and dissociation rates with the VCAM-1 coated surface. For control experiments, free peptides at a concentration of 6 mg/mL were flowed over the surface for 20 min at a rate of 2 μL/min prior to introduction of nanoclusters to saturate the binding sites. Binding parameters were determined from a 1:1 Langmuir binding model[20] with BIAevaluation software version 4.1.

2.6. MR Relaxivity Characterization.

A spin echo pulse sequence was used on a 3 T Siemens Magnetom Trio scanner (Siemens AG, Erlangen, Germany) to produce phantom MR images of SPION clusters suspended in water. For MR imaging, the echo time (TE) ranged from 12 to 490 ms, while the repetition time (TR) was kept at 1200 ms for all images. Signal intensities were measured with ImageJ, and the T_2 relaxation was determined by least-squares curve fitting of signal as a function of TE.[18] When the samples are imaged with longer echo times, the signal intensity for a fully relaxed image was obtained, thus enabling a more accurate fit to determine T_2. After imaging, phantoms were digested in nitric acid, and the iron content was measured with inductively coupled plasma optical emission spectroscopy (ICP-OES, PerkinElmer Optima 2000 DV, Norwalk, CT). Relaxivity was then determined by linear regression of the relaxation rate ($1/T_2$) versus iron content.

2.7. Analysis of Saturation Magnetization.

SPION magnetization was examined with a magnetometer (MPMS, Quantum Design) as previously described.[18] The saturation magnetization was determined to be 71 emu/g, which yielded a calculated maximum relaxivity for the SPIONs of 742 mM^{-1} s^{-1}.

3.   RESULTS AND DISCUSSION

3.1. Fabrication of SPION Clusters.

As the first step, HPGs with molecular weights of 3000 and 50 000 g/mol, referred to as HPG$_{3k}$ and HPG$_{50k}$, respectively, were prepared by varying the ratio of glycidol to an anionic ring opening initiator. The resultant HPGs were alkylated with octadecyl chains by reaction with bromooctadecane. The HPG$_{3k}$ was found to have an average of three octadecyl groups per macromolecule, designated HPG$_{3k}$-g-C$_{18}$(3), whereas its HPG$_{50k}$ counterpart had 15 chains, termed HPG$_{50k}$-g-C$_{18}$(15). Separately, oleic acid-coated SPIONs were fabricated via the high-temperature thermal decomposition of iron oleate. These SPIONs had an average core diameter of 5 nm, as confirmed by images captured with TEM.[21]

Clusters of SPIONs were fabricated by emulsifying SPIONs dispersed in chloroform with HPG dissolved in deionized water (Figure 1a). The clusters had a spherical morphology when HPGs with unary molecular weight were used to form the SPION clusters (Figures 1a and b). Interestingly, however, when the aqueous phase of the emulsion consisted of a binary mixture of the HPG$_{50k}$-g-C$_{18}$(15) and HPG$_{3k}$-g-C$_{18}$(3), there was a notable change in morphology (Figures 1a and b). Specifically, as f_{3k}, defined in eq 1, increased, the clusters became elongated.

$$f_{3k} = \frac{n_{3k}}{n_{3k} + n_{50k}}$$

(1)

Here, n_{3k} and n_{50k} are defined as the molar amount of HPG$_{3k}$-g-C$_{18}$(3) and HPG$_{50k}$-g-C$_{18}$(15), respectively. Notably, at a critical f_{3k} value of 0.75, the SPION clusters were maximally extended, forming worm-like structures (Figure 1b). These worm-like clusters had an average aspect ratio of 10. More than 50% of the SPIONs took the form of worm-like cluster under these conditions, whereas at other f_{3k} values, such as 0.25 and 0.50, only approximately 15% of the SPION clusters presented an elongated shape, with an average aspect ratio of 4 (Figure 1b). The distribution of aspect ratios in these samples can be found in Figure S3.

It is proposed that the morphological changes of the SPION clusters arise from the molecular weight mismatch of the HPGs, independent of the degree of alkylation. For example, the mixture of HPG$_{50k}$ and HPG$_{3k}$, both of which are conjugated with two C$_{18}$ chains per molecule, still resulted in assemblies with a worm-like appearance when f_{3k} was 0.75 (Figure 1c). In contrast, mixing HPG$_{3k}$ with two different degrees of alkylation, namely HPG$_{3k}$-g-C$_{18}$(3) and HPG$_{3k}$-g-C$_{18}$(5), did not result in a worm-like cluster (Figure

1d). It was also demonstrated that the difference in the molecular weight of the HPGs is a key factor in forming the worm-like SPION clusters. Alkylated but intermediately sized HPGs with a molecular weight of 8000 g/mol, $HPG_{8k}\text{-}g\text{-}C_{18}(2)$, were not able to form worm-like SPION clusters when mixed with either $HPG_{3k}\text{-}g\text{-}C_{18}(3)$ or $HPG_{50k}\text{-}g\text{-}C_{18}(15)$, which may be due to a small difference in size (Figures 1e and f). Aqueous suspensions of these nanoclusters remained stable for over a month at room temperature. Addition of these nanoclusters into phosphate buffered saline (PBS) supplemented with 10% serum at 37 °C did not result in any morphological changes or aggregation (Figure S4).

Additionally, the SPIONs themselves served to promote the formation of worm-like structures.[22] When f_{3k} was 0.75, the $HPG_{3k}\text{-}g\text{-}C_{18}(5)$ and $HPG_{50k}\text{-}g\text{-}C_{18}(15)$ created a self-assembled structure by themselves without SPIONs. However, the vast majority of the polymeric structures produced were spherical (Figure S5).

We postulate that formation of the worm-like SPION cluster results from the packing behavior of HPG_{50k} and HPG_{3k} by analogy to classical arguments for high-curvature spherical vs lower-curvature worm-like micelles. Coarse-grained simulations depicted in the Supporting Information highlight geometric differences between the alkylated HPG_{50k} and HPG_{3k}, in particular the presence of voids in the expanded HPG_{50k} unit (Figure 2a). We suggest that HPGs self-assemble in a "wedge" geometry on the spherical SPION, in which the HPG unit can be highly stretched to accommodate the size disparity compared to the hydrophobic alkyl chains. Such molecular stretching would drive an increase in the curvature and form the spherical SPION cluster (Figure 2b). In contrast, when the binary mixture of HPG_{3k} and HPG_{50k} with an intermediate f_{3k} (e.g., 0.75) induces the SPION nanocluster, it is likely that HPG_{3k} readily fills the interstitial volume between the HPG_{50k} molecules (Figure 2c). HPG_{3k} spaces out the large HPG_{50k} molecules, thereby decreasing the HPG-induced curvature and forming worm-like SPION clusters at intermediate f_{3k}.

3.2. MR Relaxivities of SPION Clusters.

According to MR images of phantom models prepared by dispersing SPIONs or SPION clusters in water, both spherical and worm-like clusters created substantial negative contrast at 0.07 mM Fe (Figure 3a). In contrast, the single SPIONs (FeREX, BioPAL Inc.) failed to generate such negative contrast even at a higher concentration of 0.14 mM Fe (Figure 3a). Measurement of T_2 molar relaxivity from the phantom images yielded a value of 675 mM^{-1} s^{-1} for the worm-like clusters, nearly reaching the theoretical maximum value, 742 mM^{-1} s^{-1}. The theoretical maximum value was calculated with saturation magnetization measured with MPMS.

The T_2 molar relaxivity of worm-like SPION clusters was slightly higher than that of spherical clusters prepared solely with the $HPG_{3k}\text{-}g\text{-}C_{18}(5)$. One explanation is that HPG_{50k} significantly increased the hydrophilicity of the cluster surface, noting that HPG_{50k} is more hydrophilic than HPG_{3k} because of the larger number of hydroxyl groups in a given volume. In contrast, the spherical cluster prepared by HPG_{3k} may present zones unoccupied by HPG because of the excluded volume effect. Another explanation could be due to size effects, as aggregate size can play a major role in relaxivity enhancement. Previous work examined the

effects of HPG molecular weight and cluster size on relaxivity.[18] Furthermore, anisotropy has been implicated in affecting molar relaxivity in other systems and could cause the worm-like clusters to have better contrast capability.[23–26] Spherical and worm-like clusters both presented relaxivities that were substantially greater than that of the single SPIONs, which yielded a relaxivity less than 200 mM^{-1} s^{-1}.

Furthermore, because our approach of tuning the morphology of the nanoclusters relies on a size mismatch of the HPG units rather than hydrophobicity, we maintained a high degree of hydrophilicity. The surface hydrophilicity is important in the design of any MRI contrast agent. In addition, the clustered nature of the SPIONs that make up the worm-like structure may prove advantageous over linearly aligned SPIONs,[27–29] as thicker clusters could allow relaxivity to be maximized within the static dephasing regime (SDR).[30,31] As a result of the hydrophilicity coupled with the high degree of clustering, the relaxivity of the clusters was higher than previous reports of elongated nanocarriers of SPIONs.[15,32,33] Additional relaxivity improvement may be possible by inducing clustering of SPIONs of a larger diameter. Whereas 5 nm is the diameter typical of commercial biomedical SPIONs such as FeREX, a core diameter of 10 nm, for example, would likely provide higher saturation magnetization and therefore could result in higher relaxivity.[34]

3.3. Targeting Efficiency of Peptide-Modified SPION Clusters.

We next modified SPION clusters with targeting ligands by conjugating VHPKQHR peptides to HPG so as to examine the ability of the HPG-SPION cluster to accumulate at simulated defective tissue sites of interest. The peptide was conjugated to an acrylate-modified HPG_{3k}-g-$C_{18}(3)$ via the terminal cysteine residue (Figure 4a). The peptide-conjugated HPG was subsequently used to induce SPION clustering. The presence of the peptide did not interfere with the morphology of the clusters (Figure 4b).

The kinetics of binding between SPION clusters and inflammatory sites was examined by measuring association and dissociation rates with VCAM-coated substrates using SPR spectroscopy. VCAM-1 receptors were immobilized on an SPR chip, and SPION clusters were introduced into the flow to examine their binding properties. The binding resonance unit (RU) for the worm-like clusters, indicative of molecular mass bound to the SPR chip, was dramatically higher than that of the spherical clusters at the same iron dose (Figure 4c). When the binding parameters are taken into account, the association rate constant, k_a, was 1 order of magnitude higher per iron dose for worm-like SPION clusters than that of spherical ones (Table 1). Additionally, the dissociation rate constant, k_d, was 2 orders of magnitude lower. As a result, the overall binding constant, a ratio of k_a to k_d, was over 3 orders of magnitude greater for the worm-like clusters (Table 1).

In addition to morphology, the importance of the targeting peptide was evaluated in control experiments using SPION nanoclusters either free of targeting peptides or peptide-conjugated clusters flowed over VCAM presaturated with peptide (Figure S6). Without targeting peptide, the binding was significantly reduced compared to binding between VCAM-1 and the peptide-conjugated worm-like HPG-SPIONs. Similarly, by occupying the binding sites of VCAM-1 prior to administration of the nanoclusters, the VHPKQHR

peptide-conjugated SPION clusters minimally adhered to the substrate. The advantage of the targeted worm-like clusters over targeted spheres is further highlighted by considering the number of peptides per iron dose. According to thermogravimetric analysis (TGA), the molar amount of peptides per iron for spherical and worm-like clusters was approximately 1:36 and 1:112, respectively, as described in the Supporting Information. In this way, despite fewer peptides per iron dose, the worm-like clusters were able to bind significantly more iron to the simulated target site in SPR experiments.

The transport mechanism presented herein mimics the way in which several strains of bacteria and parasites have developed rod-shaped or filamentous morphologies to maximize contact surface area with the endothelium of their host under shear forces of blood flow.[35] Others have directly used such structures as templates for assembling nanoparticles to increase the number of particles immobilized per binding event.[36] Similarly, our approach was able to bring a large number of SPION clusters to a model target site compared with that using spherical SPION clusters. Additionally, the elongated morphology may allow for extended circulation in vivo compared to spherical structures,[26,37] which could also promote accumulation at sites of inflammation.

4.   CONCLUSION

Taken together, this study demonstrated SPION clusters with worm-like morphology and HPG-induced hydrophilic surfaces present superior MR relaxivity compared to that of a single SPION, and a targetability higher than that of spherical SPION clusters. In future studies, the worm-like structures may be purified from their spherical counterparts to yield a uniform population with enhanced targetability. Additionally, by understanding the specific parameters that result in the wormlike clusters, it may be possible to fabricate populations that are more monomodal. In this way, efforts to study this mechanism of self-assembly will be critical in further improving these targeted clusters. Hence, this study also has the potential to substantially enhance imaging-based diagnostic capabilities. We also believe that the assembly strategy presented here could be readily extended to other nanoparticle types and is therefore broadly applicable to colloidal systems.

Supplementary Material

Refer to Web version on PubMed Central for supplementary material.

ACKNOWLEDGMENTS

REFERENCES

(1). Choi HS; Liu W; Liu F; Nasr K; Misra P; Bawendi MG; Frangioni JV Design Considerations for Tumour-Targeted Nanoparticles. Nat. Nanotechnol 2010, 5, 42–47. [PubMed: 19893516]

(2). Byrne JD; Betancourt T; Brannon-Peppas L Active Targeting Schemes for Nanoparticle Systems in Cancer Therapeutics. Adv. Drug Delivery Rev 2008, 60, 1615–1626.

(3). Yun Y; Cho YW; Park K Nanoparticles for Oral Delivery: Targeted Nanoparticles with Peptidic Ligands for Oral Protein Delivery. Adv. Drug Delivery Rev 2013, 65, 822–832.

(4). Gu F; Zhang L; Teply BA; Mann N; Wang A; Radovic-Moreno AF; Langer R; Farokhzad OC Precise Engineering of Targeted Nanoparticles by Using Self-Assembled Biointegrated Block Copolymers. Proc. Natl. Acad. Sci. U. S. A 2008, 105, 2586–2591. [PubMed: 18272481]

(5). Davis ME; Zuckerman JE; Choi CHJ; Seligson D; Tolcher A; Alabi CA; Yen Y; Heidel JD; Ribas A Evidence of RNAi in Humans from Systemically Administered siRNA via Targeted Nanoparticles. Nature 2010, 464, 1067–1070. [PubMed: 20305636]

(6). Lai M-H; Jeong JH; DeVolder RJ; Brockman C; Schroeder C; Kong H Ellipsoidal Polyaspartamide Polymersomes with Enhanced Cell-Targeting Ability. Adv. Funct. Mater 2012, 22, 3239–3246. [PubMed: 23976892]

(7). Chen J; Clay NE; Park N.-h.; Kong H Non-Spherical Particles for Targeted Drug Delivery. Chem. Eng. Sci 2015, 125, 20–24. [PubMed: 25838583]

(8). Blanazs A; Armes SP; Ryan AJ Self-Assembled Block Copolymer Aggregates: From Micelles to Vesicles and Their Biological Applications. Macromol. Rapid Commun 2009, 30, 267–277. [PubMed: 21706604]

(9). Cheng H; Yuan X; Sun X; Li K; Zhou Y; Yan D Effect of Degree of Branching on the Self-Assembly of Amphiphilic Hyper-branched Multiarm Copolymers. Macromolecules 2010, 43, 1143–1147.

(10). Chhatre A; Duttagupta S; Thaokar R; Mehra A Mechanism of Nanorod Formation by Wormlike Micelle-Assisted Assembly of Nanospheres. Langmuir 2015, 31, 10524–10531. [PubMed: 26348207]

(11). Zhang L; Eisenberg A Multiple Morphologies of "Crew-Cut" Aggregates of Polystyrene-B-Poly(Acrylic Acid) Block Copolymers. Science 1995, 268, 1728–1731. [PubMed: 17834990]

(12). Rajagopal K; Mahmud A; Christian DA; Pajerowski JD; Brown AEX; Loverde SM; Discher DE Curvature-Coupled Hydration of Semicrystalline Polymer Amphiphiles Yields Flexible Worm Micelles but Favors Rigid Vesicles: Polycaprolactone-Based Block Copolymers. Macromolecules 2010, 43, 9736–9746. [PubMed: 21499509]

(13). Won Y-Y; Davis HT; Bates FS Giant Wormlike Rubber Micelles. Science 1999, 283, 960–963. [PubMed: 9974383]

(14). Wang L; Neoh KG; Kang ET; Shuter B Multifunctional Polyglycerol-Grafted $Fe_3O_4@SiO_2$ Nanoparticles for Targeting Ovarian Cancer Cells. Biomaterials 2011, 32, 2166–73. [PubMed: 21146869]

(15). Yang X; Grailer JJ; Rowland IJ; Javadi A; Hurley SA; Steeber DA; Gong S Multifunctional SPIO/DOX-Loaded Wormlike Polymer Vesicles for Cancer Therapy and MR Imaging. Biomaterials 2010, 31, 9065–73. [PubMed: 20828811]

(16). Smith CE; Shkumatov A; Withers SG; Yang B; Glockner JF; Misra S; Roy EJ; Wong C-H; Zimmerman SC; Kong H A Polymeric Fastener Can Easily Functionalize Liposome Surfaces with Gadolinium for Enhanced Magnetic Resonance Imaging. ACS Nano 2013, 7, 9599–9610. [PubMed: 24083377]

(17). Nahrendorf M; Jaffer FA; Kelly KA; Sosnovik DE; Aikawa E; Libby P; Weissleder R Noninvasive Vascular Cell Adhesion Molecule-1 Imaging Identifies Inflammatory Activation of Cells in Atherosclerosis. Circulation 2006, 114, 1504–1511. [PubMed: 17000904]

(18). Smith CE; Ernenwein D; Shkumatov A; Clay NE; Lee JY; Melhem M; Misra S; Zimmerman SC; Kong H Hydrophilic Packaging of Iron Oxide Nanoclusters for Highly Sensitive Imaging. Biomaterials 2015, 69, 184–190. [PubMed: 26291408]

(19). Kim BH; Lee N; Kim H; An K; Park YI; Choi Y; Shin K; Lee Y; Kwon SG; Na HB; Park JG; Ahn TY; Kim YW; Moon WK; Choi SH; Hyeon T Large-Scale Synthesis of Uniform and

Extremely Small-Sized Iron Oxide Nanoparticles for High-Resolution T-1 Magnetic Resonance Imaging Contrast Agents. J. Am. Chem. Soc 2011, 133, 12624–12631. [PubMed: 21744804]

(20). Kortt AA; Nice E; Gruen LC Analysis of the Binding of the Fab Fragment of Monoclonal Antibody Nc10 to Influenza Virus N9 Neuraminidase from Tern and Whale Using the Biacore Biosensor: Effect of Immobilization Level and Flow Rate on Kinetic Analysis. Anal. Biochem 1999, 273, 133–41. [PubMed: 10452809]

(21). Clay N; Baek K; Shkumatov A; Lai M-H; Smith CE; Rich M; Kong H Flow-Mediated Stem Cell Labeling with Superparamagnetic Iron Oxide Nanoparticle Clusters. ACS Appl Mater. Interfaces 2013, 5, 10266–10273. [PubMed: 24033276]

(22). Zhu J; Hayward RC Spontaneous Generation of Amphiphilic Block Copolymer Micelles with Multiple Morphologies through Interfacial Instabilities. J. Am. Chem. Soc 2008, 130, 7496–7502. [PubMed: 18479130]

(23). Zhao Z; Zhou Z; Bao J; Wang Z; Hu J; Chi X; Ni K; Wang R; Chen X; Chen Z; Gao J Octapod Iron Oxide Nanoparticles as High-Performance T2 Contrast Agents for Magnetic Resonance Imaging. Nat. Commun 2013, 4, 2266. [PubMed: 23903002]

(24). Zhou Z; Zhao Z; Zhang H; Wang Z; Chen X; Wang R; Chen Z; Gao J Interplay between Longitudinal and Transverse Contrasts in Fe3O4 Nanoplates with (111) Exposed Surfaces. ACS Nano 2014, 8, 7976–7985. [PubMed: 25093532]

(25). Wyss PP; Lamichhane S; Rauber M; Thomann R; Kramer KW; Shastri VP Tripod USPIONs with High Aspect Ratio Show Enhanced T2 Relaxation and Cytocompatibility. Nanomedicine (London U. K.) 2016, 11, 1017–1030.

(26). Park J-H; von Maltzahn G; Zhang L; Derfus AM; Simberg D; Harris TJ; Ruoslahti E; Bhatia SN; Sailor MJ Systematic Surface Engineering of Magnetic Nanoworms for in Vivo Tumor Targeting. Small 2009, 5, 694–700. [PubMed: 19263431]

(27). Gossuin Y; Disch S; Vuong QL; Gillis P; Hermann RP; Park J-H; Sailor MJ NMR Relaxation and Magnetic Properties of Superparamagnetic Nanoworms. Contrast Media Mol. Imaging 2010, 5, 318–322. [PubMed: 21190269]

(28). Park J-H; von Maltzahn G; Xu MJ; Fogal V; Kotamraju VR; Ruoslahti E; Bhatia SN; Sailor MJ Cooperative Nanomaterial System to Sensitize, Target, and Treat Tumors. Proc. Natl. Acad. Sci. U. S. A 2010, 107, 981–986. [PubMed: 20080556]

(29). Lo JH; von Maltzahn G; Douglass J; Park J-H; Sailor MJ; Ruoslahti E; Bhatia SN Nanoparticle Amplification via Photothermal Unveiling of Cryptic Collagen Binding Sites. J. Mater. Chem. B 2013, 1, 5235–5240. [PubMed: 24177171]

(30). Yablonskiy DA; Haacke EM Theory of NMR Signal Behavior in Magnetically Inhomogeneous Tissues: The Static Dephasing Regime. Magn. Reson. Med 1994, 32, 749–763. [PubMed: 7869897]

(31). Pöselt E; Kloust H; Tromsdorf U; Janschel M; Hahn C; Maßlo C; Weller H Relaxivity Optimization of a PEGylated Iron-Oxide-Based Negative Magnetic Resonance Contrast Agent for T2-Weighted Spin–Echo Imaging. ACS Nano 2012, 6, 1619–1624. [PubMed: 22276942]

(32). Park J-H; von Maltzahn G; Zhang L; Schwartz MP; Ruoslahti E; Bhatia SN; Sailor MJ Magnetic Iron Oxide Nanoworms for Tumor Targeting and Imaging. Adv. Mater 2008, 20, 1630–1635. [PubMed: 21687830]

(33). Wang G; Inturi S; Serkova NJ; Merkulov S; McCrae K; Russek SE; Banda NK; Simberg D High-Relaxivity Superparamagnetic Iron Oxide Nanoworms with Decreased Immune Recognition and Long-Circulating Properties. ACS Nano 2014, 8, 12437–49. [PubMed: 25419856]

(34). Jun Y.-w.; Huh Y-M; Choi J.-s.; Lee J-H; Song H-T; Kim K-Y; Yoon S; Kim K-S; Shin J-S; Suh J-S; Cheon J. Nanoscale Size Effect of Magnetic Nanocrystals and Their Utilization for Cancer Diagnosis via Magnetic Resonance Imaging. J. Am. Chem. Soc 2005, 127, 5732–5733. [PubMed: 15839639]

(35). Young KD The Selective Value of Bacterial Shape. Microbiol. Mol. Biol. Rev 2006, 70, 660–703. [PubMed: 16959965]

(36). Ghosh D; Lee Y; Thomas S; Kohli AG; Yun DS; Belcher AM; Kelly KA M13-Templated Magnetic Nanoparticles for Targeted in Vivo Imaging of Prostate Cancer. Nat. Nanotechnol 2012, 7, 677–682. [PubMed: 22983492]

(37). Geng Y; Dalhaimer P; Cai S; Tsai R; Tewari M; Minko T; Discher DE Shape Effects of Filaments Versus Spherical Particles in Flow and Drug Delivery. Nat. Nanotechnol 2007, 2, 249–255. [PubMed: 18654271]
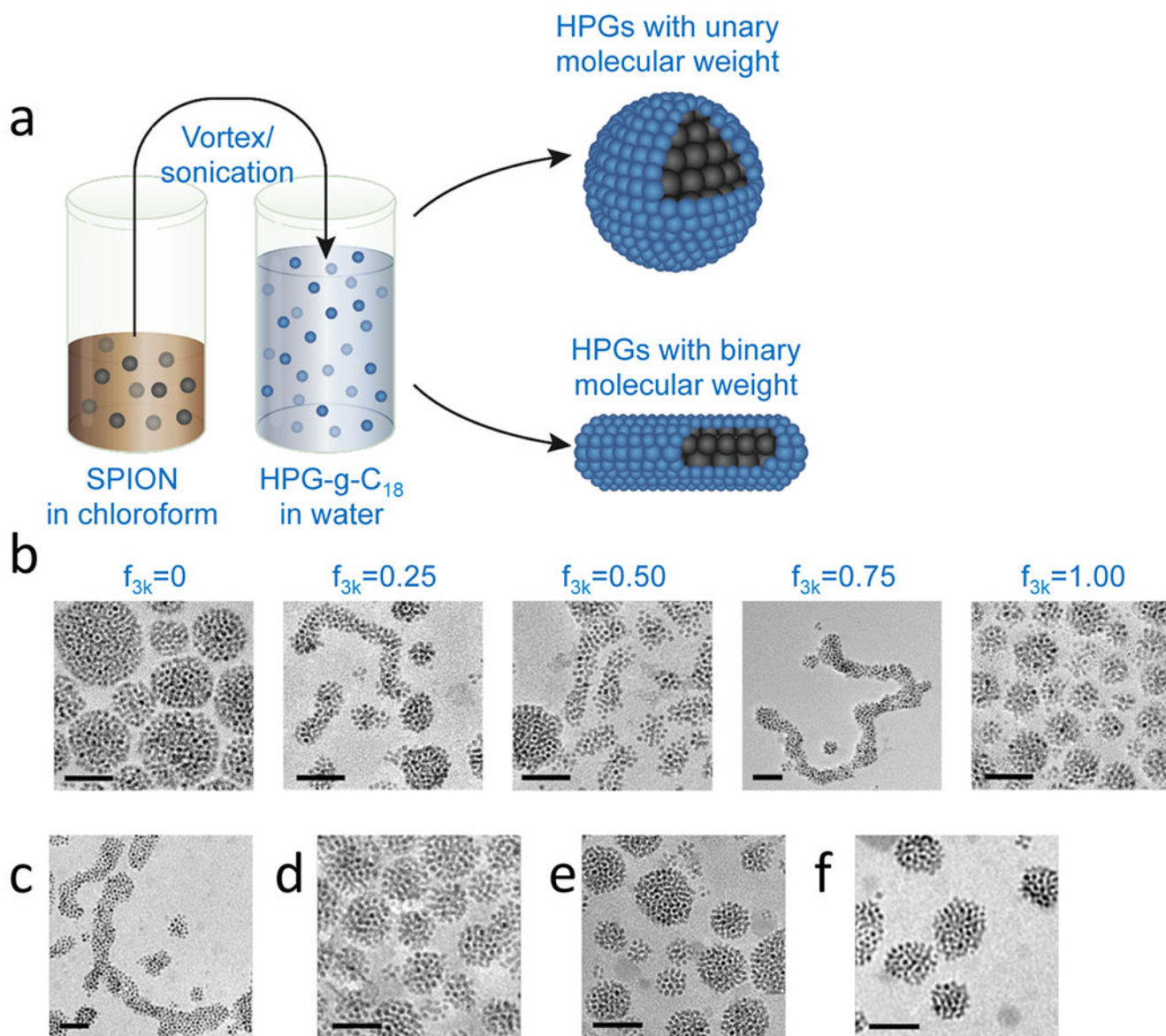
Figure 1.
Morphological control of SPION clusters. (a) Schematic describing the emulsification process to fabricate SPION clusters with controlled shapes. The oleic acid-capped SPIONs suspended in chloroform were emulsified with HPG-g-C$_{18}$ of controlled molecular weight dissolved in water. (b) TEM images showing the sphere-to-worm transition of SPION nanoclusters controlled by f_{3k}. As HPGs with MWs of 3000 and 50 000 g/mol were incorporated into water for the emulsification, the resultant SPION clusters became elongated with maximal length occurring at a 3:1 HPG$_{3k}$-g-C$_{18}$(3):HPG$_{50k}$-g-C$_{18}$(15) ratio. (c) A 3:1 ratio of low:high molecular weight HPG still resulted in worm-like clusters when both had an average of two C$_{18}$ chains per molecule. (d) Alkylated HPG$_{3k}$ was unable to produce worm-like clusters by varying only the degree of alkylation. Similarly, using

an intermediately sized HPG, HPG_{8k}-g-$C_{18}(2)$, resulted only in spheres when mixed with alkylated (e) HPG_{3k} and (f) HPG_{50k}. All scale bars represent 50 nm.
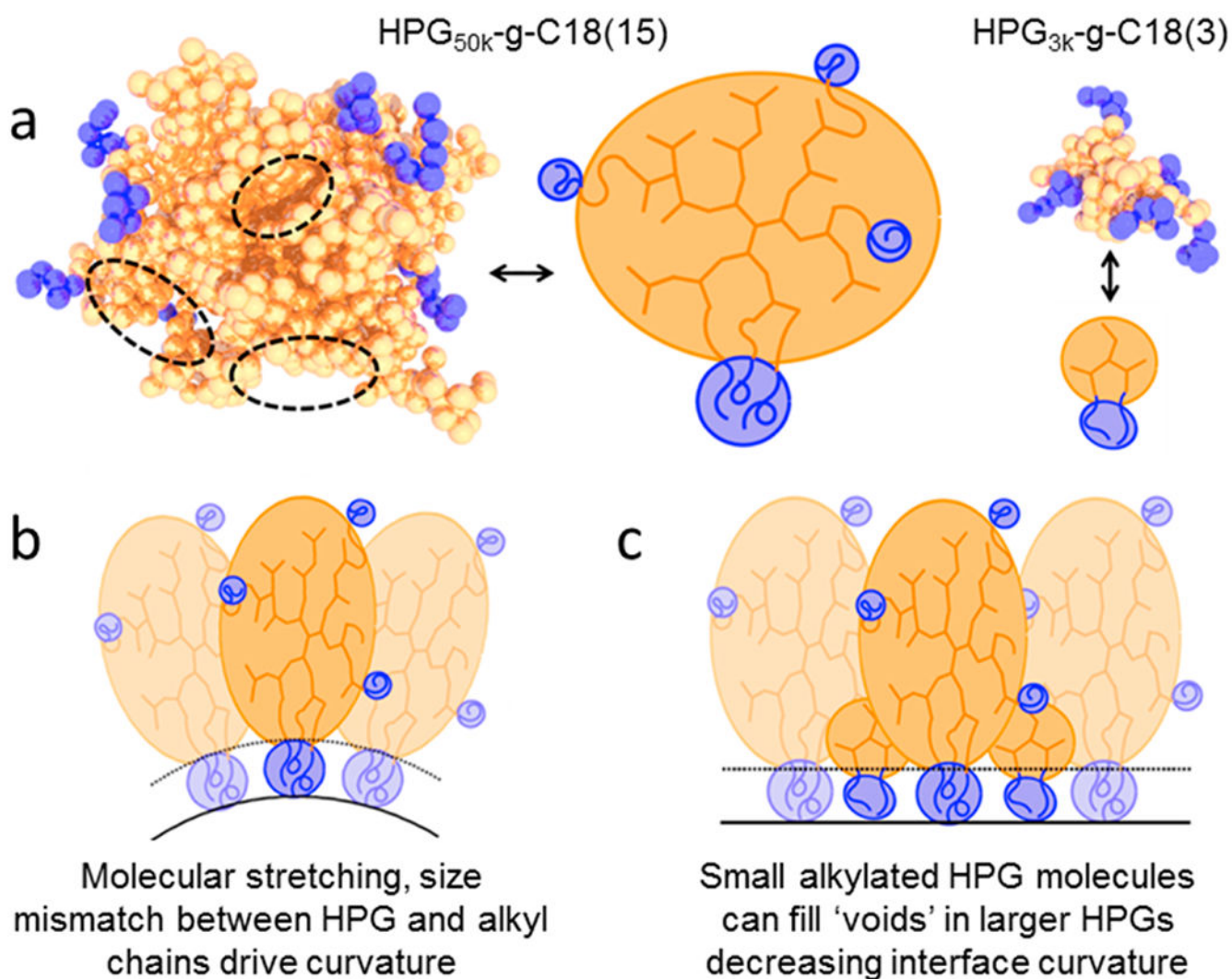
Figure 2.
Suggested mechanism of worm-like SPION cluster formation. (a) Simulated images demonstrating the structure of alkylated HPG_{50k} and HPG_{3k} along with simplified representations. We note the presence of voids in the hyperbranched conformation (dotted, black circles). (b) HPG_{50k} and alkyl components drive curvature, leading to spherical SPION clusters. (c) Introduction of smaller HPG_{3k} molecules will fill voids in HPG_{50k} molecules, decreasing curvature and allowing for worm-like SPION clusters.
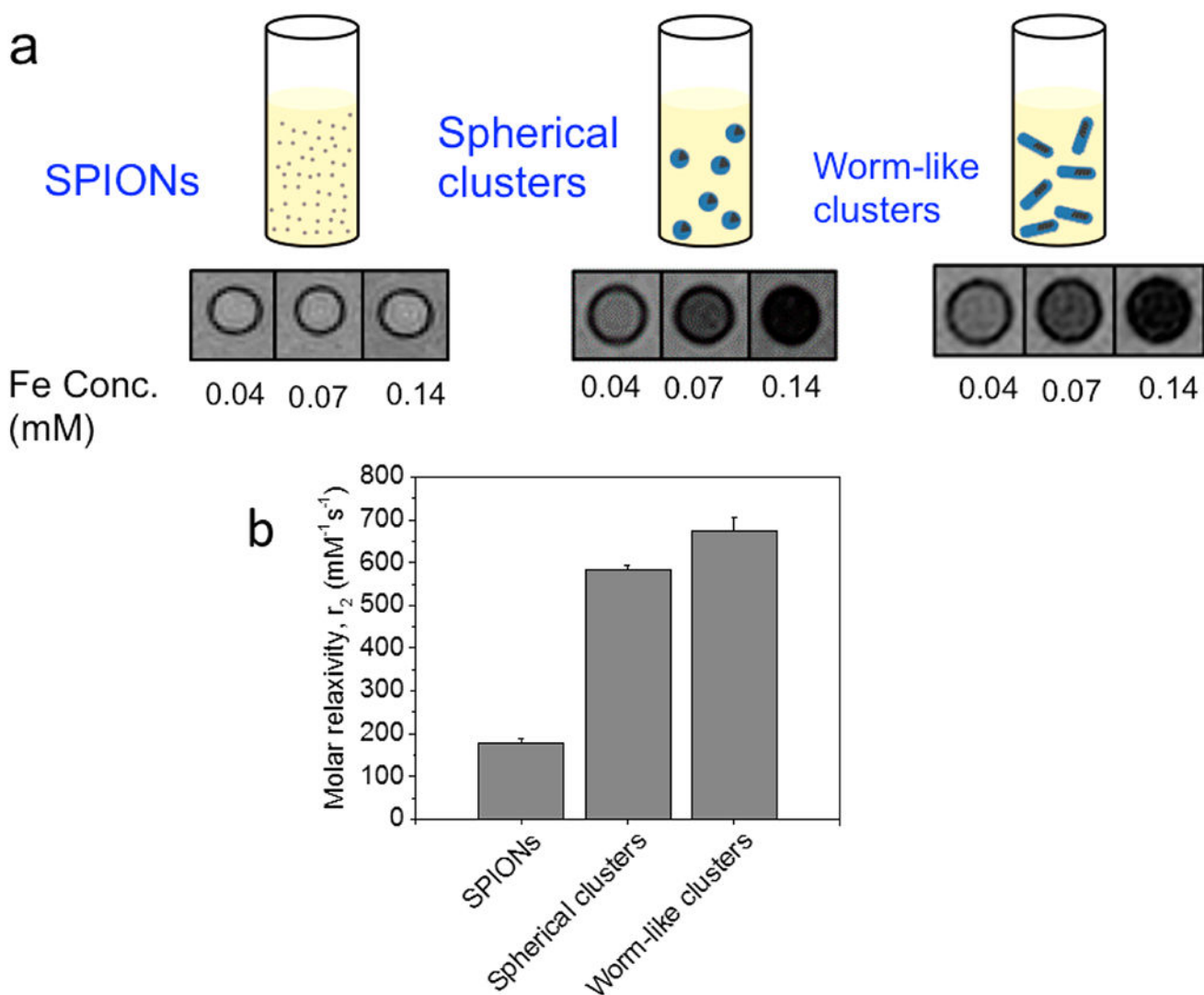
Figure 3.
Analysis of MR relaxivity of SPION clusters. (a) MR images of the phantom model prepared with SPIONs, spherical clusters, and worm-like clusters dispersed in water. (b) MR relaxivity of SPION clusters. The T_2 molar relaxivity of worm-like clusters was slightly higher than that of spherical clusters; however, resultant differences in contrast capability at given Fe concentrations were minimal. Error bars represent standard deviation of the fit parameter.
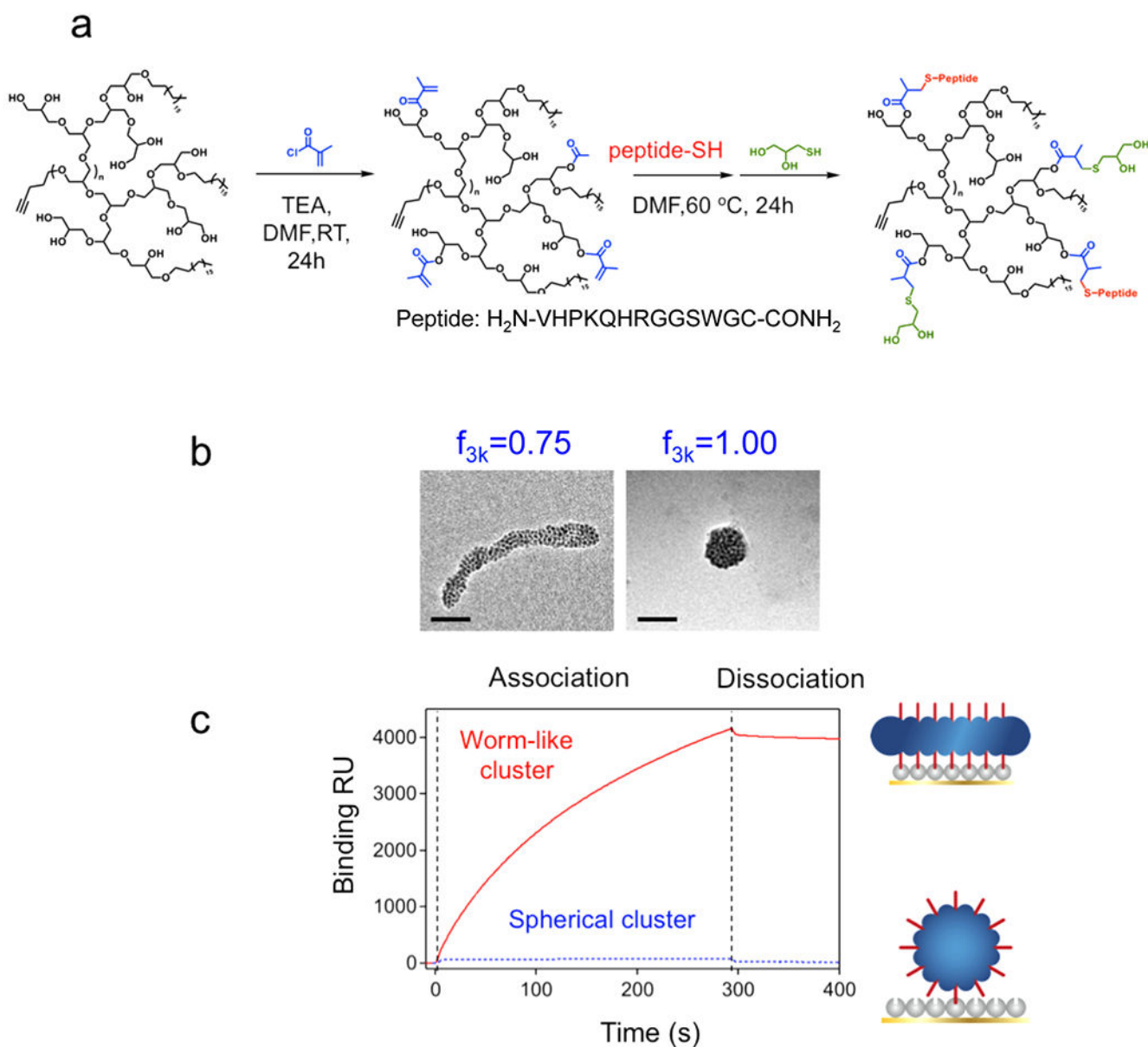
Figure 4.

Shape-controlled adhesion properties of the SPION clusters. (a) Conjugation of the VCAM-1 targeting peptide VHPKQHR to the alkylated HPG backbone. (b) Addition of the VHPKQHR peptide did not interfere with cluster formation, as SPIONs formed a worm-like cluster at f_{3k} of 0.75, while they formed a spherical cluster at f_{3k} of 1. Scale bars represent 50 nm. (c) SPR kinetic binding analysis of targeted worm-like (red, solid curve) and spherical (blue, dotted curve) nanoclusters during association and dissociation with VCAM-1 receptors.

Table 1.

Kinetic Binding Values for the Association and Dissociation between Nanoclusters and VCAM-Immobilized Substrate as Determined by SPR Spectroscopy[a]

morphology of targeted cluster	association rate constant k_a (M^{-1} s^{-1})	dissociation rate constant k_d (s^{-1})	binding constant K_A (M^{-1})
spherical	1.0	1.3×10^{-3}	7.7×10^2
worm-like	14.7	1.5×10^{-5}	1.0×10^6

[a]Values are given per molar concentration of iron.